Mechanical properties and numerical modeling of Fabric Reinforced Cementitious Matrix (FRCM) systems for strengthening of masonry structures

Francesca Giulia Carozzi, Gabriele Milani *, Carlo Poggi

Department of Architecture, Built Environment and Construction Engineering (ABC), Politecnico di Milano, Piazza Leonardo da Vinci 32, 20133 Milano, Italy

1. Introduction

Even the recent earthquake that occurred in Italy in May 2012 indicated that historical buildings, essentially constituted by masonry structures, are scarcely resistant to horizontal loads and therefore highly vulnerable to seismic actions. Such behavior is a common issue of masonry buildings in many countries worldwide and is essentially due to the low strength of the mortar joints when loaded out-of-plane.

Conventional retrofitting techniques, such as external reinforcement with steel plates, surface concrete coating and welded steel meshes, have proven to be complex, time expensive and add considerable mass to the structure which may increase the inertia forces induced by an earthquake.

Therefore, the use of FRP (Fiber-Reinforced Polymers) strips as reinforcements instead of conventional methods seems a suitable solution for the seismic upgrading, thanks to the limited invasiveness, speed of execution, and good performance at failure [1–7]. The FRP strengthening technique entails however several drawbacks, as for instance low vapor permeability, poor behavior at elevated temperatures, incompatibility of resins on different substrate materials, relative high cost of epoxy resins, no reversibility of the installation [8].

The use of inorganic matrices is a valid alternative to these problems [7]. It is well known, however, that cement based

* Corresponding author. Tel.: +39 022399 4290; fax: +39 022399 4220.
E-mail address: gabriele.milani@polimi.it (G. Milani).

Nomenclature

A_L	perimeter of the yarn
A_{FRP}	transversal area of a single yarn
c_I	peak strength of the interface between yarn and mortar
c_{II}	residual strength between yarn and mortar
δ	displacement
e	eccentricity of the load, 150 mm anchorage length
e_0	prescribed eccentricity in the numerical models (1D and 3D)
E_{FRP}	Young modulus of Glass Fiber grid
f	tangential unitary force between yarn and mortar (N/mm)
F	force
F_i	forces in the single yarns
F_u	ultimate strength
F_{u2}	residual strength of the overall system
$f_{u\text{-FRP}}$	ultimate value of stress in a yarn
L	distance between two contiguous yarns
L_b	length of the bonded region
L_u	length of the unbounded region
L_{2-3}	length of an interface finite element between nodes 2 and 3
n_{el}	number of elements
n_{in}	number of interfaces
n_y	number of yarns
k_n	axial elastic stiffness of the yarn
k_t	Tangential elastic stiffness of yarn–mortar interface
$\mathbf{K}_{el}$	assembled elastic stiffness matrix
$\mathbf{K}_{ep}$	interfaces hardening moduli matrix
K_T	stiffness of the mechanical system
u_i	displacement of the single yarn
u_x^E, u_y^E, u_z^E	kinematic variables: three centroid displacements
u_t^{Ei}	absolute displacement along **t** of element *Ei*
t	direction versor
Δ_{b1}	yarn–mortar interface, slip value corresponding to the first strength drop
Δ_{b2}	yarn–mortar interface, slip value corresponding to the second strength drop
ΔL_u	overall displacement due to the unbounded part
ΔL_b	overall displacement of the bonded part
Δs^{P1}	tangential slip of point *P*1
Δs_e	displacement at the elastic limit
Δs_{u1}	displacement value reached when the tangential force shifts from peak to residual value
Δs_{u2}	displacement value reached in correspondence of a drop of tangential force from the residual value to zero
$\Delta\mathbf{F}$	vector of elements force and moment increments
$\Delta\mathbf{U}_{el}$	vector of elements displacement and rotation increments
$\Delta\boldsymbol{\lambda}^+$ and $\Delta\boldsymbol{\lambda}^-$	assembled plastic multiplier increment vectors
ε_u	ultimate axial strain of the GFRP yarn
ε_e	elastic axial strain of the GFRP yarn
ε_n	continuum strain
λ	parameter entering in the elastic equation of the yarn–mortar interface
ξ	geometric parameter entering in the elastic equation of the yarn–mortar interface
ϑ	rotation of the rigid device connecting perpendicularly the three yarns in correspondence of their extremes free to translate
σ	tensile stress
τ	tangential stress
Φ_x^E, Φ_y^E, Φ_z^E	kinematic variables: three rotations around the centroid

materials have low tensile strength and must be reinforced with tensile resistant components. Typically, steel bars are used in the conventional reinforced concrete (RC). In the last two decades innovative types of reinforcements have been introduced: short fibers (FRC, Fiber Reinforced Concrete [9]) and continuous fibers in a fabric form (TRC, Textile Reinforced Concrete). Typical applications are cladding panels, exterior sidings, shells, roofing or flooring tiles. Fabric Reinforced Cementitiuos Matrix (FRCM) composites represent a particular type of TRC [10] where a dry-fiber fabric is applied to a structure through a cementitious mortar enriched with short fibers. And they are specifically used for strengthening of structures. The mechanical properties of FRCMs depend on the bond between the fibers and the matrix and may vary if the yarns of the fabrics are pre impregnated with resin [11,12]. FRCM are often used to repair and strengthen existing structures as an alternative to FRP composites [13]. When compared with FRP composites, FRCM exhibits several advantages, as a greater resistance to high temperatures and ultraviolet radiations, as well as a better compatibility with the substrates [14].

On the other hand, FRCM composites have some drawbacks, as for instance the lower levels of adhesion between the yarns and the matrix and the fact that they must be made either with alkaline resistant glass fibers or the yarns must be protected with suitable coatings.

The typical failure mode of FRP is the debonding of the reinforcement from the substrate with a brittle behavior [8,15,16], while FRCM materials can present more complex failure modes. The typical stress–strain behavior of a FRCM is a tri-linear curve, with a first phase that increases linearly according to the Young's modulus of the mortar, a second phase where the cracks in the mortar start to grow, and a last phase in which the mortar is fully cracked and the curve assumes the same slope of the stiffness of the fabric [17].

Despite the great importance and the increasing diffusion of such innovative strengthening technique, at present no numerical models devoted to the prediction of the behavior or FRCM masonry reinforced specimens or structural elements are at disposal and limited experimental data are available. In this context, the present work studies in detail the strengthening of masonry structures with FRCM from both an experimental and numerical point of view. The experimental investigation, partially presented in [18], includes various activities, starting from the characterization of the Glass Fiber (GF) grid and two types of mortars (a cementitious and a lime based mortar). Similar series of tests were performed on FRP reinforced specimens by other authors to evaluate the capabilities of the strengthening system, including (1) push–pull tests on double lap reinforcements applied to a single brick [15,19], (2) a series of tensile tests on the reinforcement applied to a pillar [20] and (3) pull-out tests on single yarns immersed in a mortar block, performed to have an insight into the interface behavior. When dealing with the reinforced single brick, three anchorage lengths are analyzed, equal respectively to 50 mm, 100 mm and 150 mm.

The numerical investigation is aimed at simulating the experiments on the reinforced single brick and the masonry pillar. The final objective is to provide a validated tool for the design and the assessment of these reinforcement systems. Two complementary tools are proposed: a simplified analytical–numerical approach to model the specific interaction of the grids with the mortar by means of interfacial tangential stresses and a sophisticated fully

3D numerical model including materials exhibiting softening [21,22]. For both models, the interface behavior between mortar and grid is based on the slip–stress curves deduced from experiment data. In both cases, quite satisfactory results are found, with a promising agreement with experimental data both in terms of global load–displacement behavior and deformed shapes near collapse. Within the full 3D numerical approach, for all cases analyzed, a debonding of the GF grid from the mortar is experienced, which reproduces well the experimental evidences.

The analytical–numerical approach appears particularly attractive for design purposes as preliminary tool, since it provides a quick estimate of the non-linear behavior of the single reinforced specimens subjected to standard Push–pull tests, and the most significant parameters (loads, eccentricities, boundary conditions, mechanical properties of the constituent materials, etc.) to be further used in more complex 3D FEM simulations.

2. Experimental investigation

In this section, the results of a wide experimental program carried out at the Materials Testing Laboratory of the Politecnico di Milano (Laboratorio Prove Materiali) are presented. The section is subdivided in four parts, representing the phases followed during the experimental program. In the first part, the mechanical characterizations of the constituent materials are presented (i.e. the glass fiber grid, the cementitious and lime base mortars, and the bricks), while in the two following sections the results of the tests conducted on the reinforced single bricks and the masonry pillar for different bond lengths for the grids are reported. Finally, the behavior of the interface between GF grid and mortar is experimentally determined. In particular, a single yarn immersed into a small block of mortar and subjected to an increasing tensile load up to failure is tested with the aim of evaluating the typical curve representing the bond slip against shear load occurring at the interface. This latter study was of particular interest to calibrate the behavior of the interface in the numerical model.

2.1. Constituent materials mechanical characterization

The results of the characterization of the reinforcement components, namely the GF grid (SikaWrap®-350G Grid), the cementitious mortar (Sika® MonoTop-722 Mur), the lime based mortar (Sika® R-I-Z) and the brick, are here presented.

2.1.1. Glass Fiber grid

Tensile tests were performed according to EN ISO 10618/2005 [23] on a single roving (GF grid protected with Styrene Butadiene Rubber) in the warp and weft directions (5 specimens were tested in each direction). The GF unbalanced grid had size equal to 17 × 12 mm, the yarn in the warp direction was characterized by 2308 Tex (g/km) and a section of 0.92 mm^2, the yarn in the weft direction was characterized by 2226 Tex (g/km) and a section of 0.90 mm^2. The woven exhibited a crimped shape in both directions.

Tensile tests were also performed on a 5 cm wide grid, even in this case in both warp and weft directions (5 specimens in each direction). Tests were carried out using two different testing machines with maximum capacities of 2 kN and 100 kN. It is worth noting that the testing machine with capacity 2 kN was used exclusively to perform tensile tests on single yarns, whereas the testing machine with 100 kN capacity was used for the remaining tests. In order to avoid local damage of the specimens during the tensile tests, special fiberglass tabs were used. The experimental results are summarized in Table 1.

Table 1
Characterization of the GF grid.

Tensile tests	Average failure load (kN)	CoV of strength (%)
Roving in the warp direction	1.11	2.7
Roving in the weft direction	1.03	1.7
Grid strip of width 5 cm (3 rovings in the warp direction)	3.36	1.3
Grid strip of width 5 cm (4 rovings in the weft direction)	4.24	2.8

2.1.2. Cementitious and lime based mortars

Two types of mortars were considered, a cementitious and a lime based mortar. The first is more suitable for structural strengthening of existing structures, whereas the latter is usually adopted for historical buildings, mainly due to compatibility issues with the substrate. In both cases, the compressive and flexural strengths were experimentally determined according to EN 1015-11 [24] (see Table 2). Six specimens were tested for both cementitious and lime based mortar.

It is evident that the cementitious matrix presents much higher strength values approximately one order of magnitude higher. This was expected and indicates that lime mortars can be used only in particular applications.

Table 2
Characterization of mortar compressive and flexural strength.

Test type	Average compression strength (N/mm^2)	Mean flexural strength (N/mm^2)
Cementitious mortar "Sika® MonoTop – 722 Mur"	27.13	8.38
Lime based mortar "Sika® R-I-Z"	2.75	1.03

2.1.3. Bricks mechanical characterization

Two types of bricks were considered, labeled as "historical block" and "standard modern" bricks respectively. The first type is more porous and less resistant. Both of them have dimensions equal to 250 × 55 × 120 mm (length × height × thickness). The following quantities were experimentally determined: compression strength through standard compression tests, elastic modulus

Table 3
Mechanical properties of the bricks.

Test type	Elastic modulus (GPa)	Compression strength (N/mm^2)	Tensile strength (N/mm^2)	*Cw*, *s* (kg/m^2 min)	Pull-off strength (MPa)
Standard	EN 14580	EN 772-1	EN 12390-6	EN 772-11	EN 1542
Historical bricks	–	22.32 (12)	1.81 (3)	–	–
Standard deviation	–	2.57	0.35	–	–
Modern bricks	12.33 (4)	68.87 (12)	6.24 (3)	1.37 (6)	3.07 (12)
Standard deviation	6.18	4.23	0.84	0.37	0.23

Note: within brackets # of samples.
Cw, *s*: coefficient of water absorption.

through direct determination into the uniaxial compression stress–strain diagram, water absorption and indirect tensile strength according to the Standards reported in Table 3. The experimental results are summarized in Table 3. These were then used in the numerical simulations described in the following sections.

2.2. Single brick reinforcements

Experimental tests were performed on push–pull double lap joints realized with a GF grid bonded to two opposite sides of a single brick, see Fig. 1. The specimens included the two types of clay bricks described above, "historic" and "modern". Modern bricks exhibited an extremely high compressive strength (68.87 MPa). These bricks were specifically selected to create specimens where the failure of the reinforcement was expected. The number and typology of tests, with information of bond length and mortar type are summarized in Table 4, both for historical and modern bricks.

Different bond lengths (50, 100 and 150 mm) were considered in order to investigate the effect of these parameters on the debonding strength. The reinforcement width was 50 mm, and the thickness of the mortar layer was 8 mm.

An MTS testing machine with the ultimate capacity of 250 kN was used and a special test rig was designed and realized to perform the double shear lap debonding test (see Fig. 1).

The main features characterizing the experimental response of the reinforced bricks (namely average initial stiffness and average failure load with their respective standard deviation, as well as observed failure mechanisms) are summarized in Table 5 for the sake of clearness.

2.2.1. Specimens with GF grid and cementitious mortar

It is known that in these types of applications the bond length has an influence both on the failure load and the failure mechanism. The failure load increased with the bond length and shorter reinforcements (5 cm and 10 cm) showed grid slippage at loads smaller than the tensile failure of the GF grid. On the contrary, for longer reinforcements a tensile failure of the GF grid without slippage (see Fig. 2) was experienced. No debonding of the reinforcement from the substrate was achieved for all the specimens with an anchorage length equal to 15 cm. The optimum bond length among those that were tested seems to be 15 cm with a mean failure load equal to 4.06 kN. The experimental load–displacement graphs obtained for the different bond lengths are summarized in Figs. 3–5 for specimens with anchorage length equal to 5, 10 and 15 cm respectively. It is evident that the ultimate strengths for 5 cm of anchorage length suffer for greater scatter, while the results in Figs. 4 and 5 are less dispersed. In these two last cases the coefficient of variation CoV of strength was equal to 6.6% and 13.6% respectively.

Finally, in Fig. 6, a comparison among experimental load displacement curves obtained at different bond lengths (5 replicates for each bond length) is represented. It is pretty evident both the increase of the ultimate load of the reinforced system when the anchorage length is increased, as well as the low ductility of the specimens with the longest reinforcement, as a consequence of the yarns rupture.

Table 4
Layout of the experimental tests.

Brick type	Reinf. type	Mortar type	Bond length (cm)	Reinf. width (cm)	# Tests
Modern	GF grid	Cement	5–10–15	5	5 per type
Historical	GF grid	Lime	10–15	5	3 per type

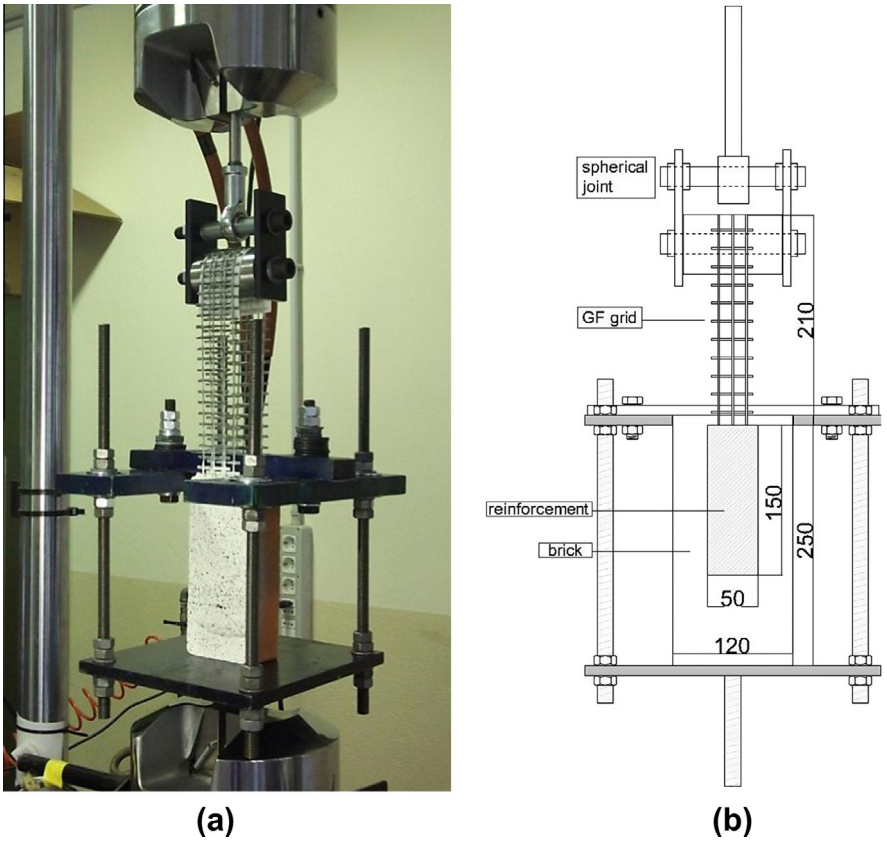

Fig. 1. Experimental set-up for debonding tests on single bricks. (a) The rig in the testing machine and (b) details of the testing rig (dimensions in mm).

Table 5
Main features of the experimentally tested reinforced bricks.

Brick type	Mortar type	Bond length (cm)	Initial stiffness (N/mm)		Failure load (kN)		Failure mode
			Average	Standard deviation	Average	Standard deviation	
Modern brick	Cement	5	679	63.7	1.06	0.17	Slippage of GFRP grid
		10	644	17.2	2.63	0.17	Slippage and tensile failure of GFRP grid
		15	670	64.4	4.06	0.55	Tensile failure of GFRP grid
Historical brick	Lime	10	396	36.9	1.50	0.23	Debonding of the reinforcement from the substrate
		15	407	11.5	1.73	0.81	Failure of mortar layer

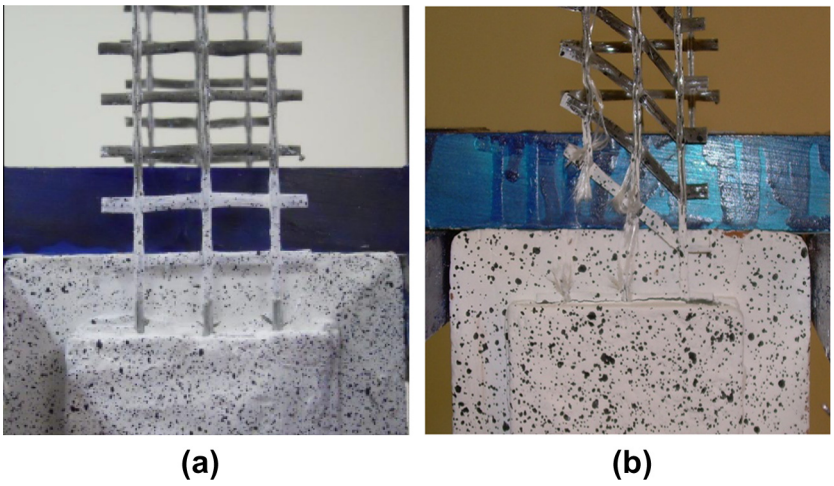

Fig. 2. GF grid embedded in the cementitious mortar. (a) Experimental failure mode for anchorage length of 50 mm, grid slippage and (b) tensile failure of the grid for anchorage length of 150 mm.

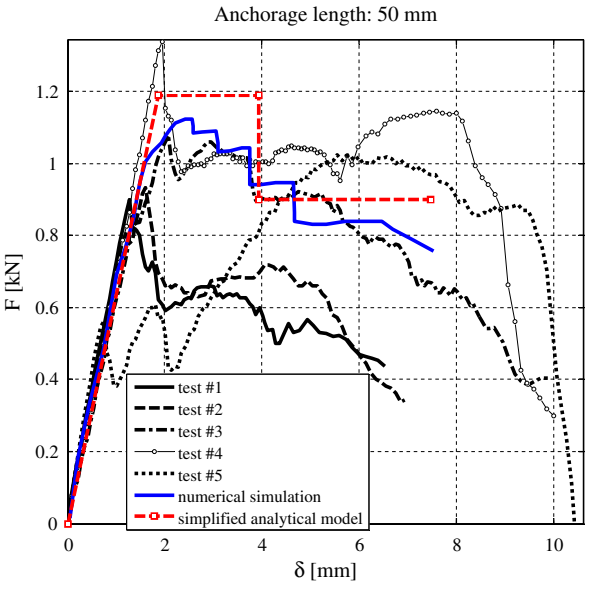

Fig. 3. Single bricks, 5 cm anchorage. Force displacement experimentally obtained curves. Comparison with numerical predictions.

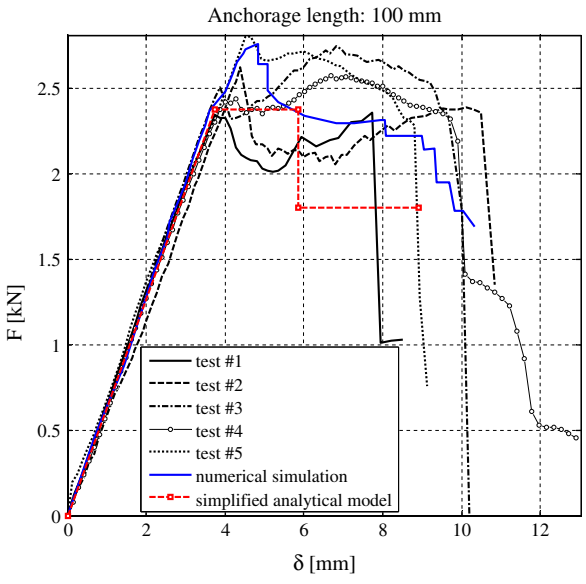

Fig. 4. Single bricks, 10 cm anchorage. Force displacement experimentally obtained curves. Comparison with numerical predictions.

2.2.2. Specimens with GF grid and lime based mortar

The specimens with lime based mortars were prepared using historical clay bricks with irregular surfaces. This was done considering that this particular type of mortar is intended for historical buildings where the cementitious matrices are often not accepted by the "Sovrintendenza ai Beni culturali" (Commission for the

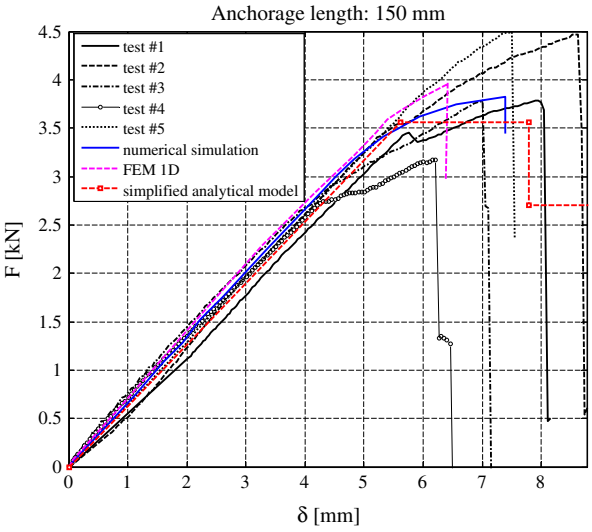

Fig. 5. Single bricks, 15 cm anchorage. Force displacement experimentally obtained curves. Comparison with numerical predictions.

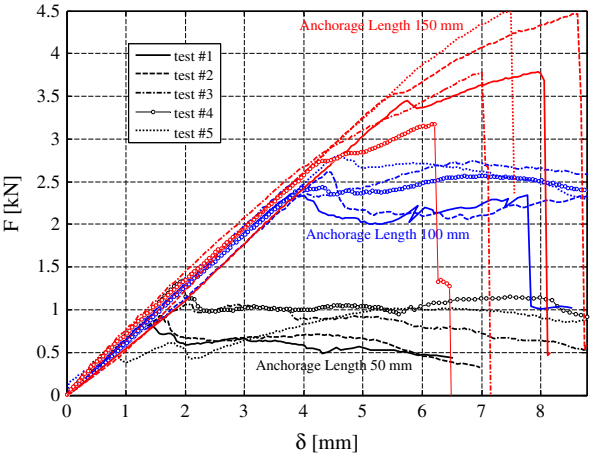

Fig. 6. Comparison among load displacement curves obtained experimentally at different anchorage lengths, single brick reinforced.

Architectural and Landscape Heritage), because considered invasive.

The experienced failure mode (see Fig. 7) was a debonding of the reinforcement from the substrate for a bond length equal to 100 mm, and tensile failure of the mortar layer for a bond length of 150 mm.

Also in this case the optimum value of the bond length seems to be 15 cm, but the corresponding failure load found is equal to 1.73 kN, sensibly lower (45%) than that found for the reinforcing system with cementitious mortar.

2.3. Reinforced masonry pillars

Tensile tests were performed on specimens realized with a GF grid and cementitious mortar bonded to both vertical sides of two masonry pillars, each one consisting of two mortar joints between three bricks (see Fig. 8a and b). The reinforcement width was 10 cm (corresponding to a strip of fabric with 6 yarns), whereas the bond length was 30 cm. The experimental failure mechanism observed was a cracking of the mortar followed by a tensile failure of the GF grid, see Fig. 8c. Debonding of the reinforcement from the substrate was never achieved (Fig. 8c). The load–displacement graphs of three replicates are shown in Fig. 9.

2.4. GFRP–mortar interface bonding behavior

In order to investigate the interface behavior between the GF grid and the cementitious mortar, three ad hoc pull-out tests were prepared.

The specimens were composed by a single yarn (extracted from the GFRP grid) included into a mortar parallelepiped with dimensions $100 \times 20 \times 10$ mm, as shown in Fig. 10. Tests were carried out using an Instron testing machine with a capacity of 2 kN. In order to avoid local damage of the GF grid during the tensile tests, special fiberglass tabs with thickness of about 2 mm were used.

Test results show common features, with load–displacement curves exhibiting an elastic phase followed by a sudden decrease of the strength (at the same mutual displacement between mortar and yarn) immediately followed by a slippage of the grid at a constant strength. Only in one case (test #2) failure of the GFRP grid (Fig. 11) was observed.

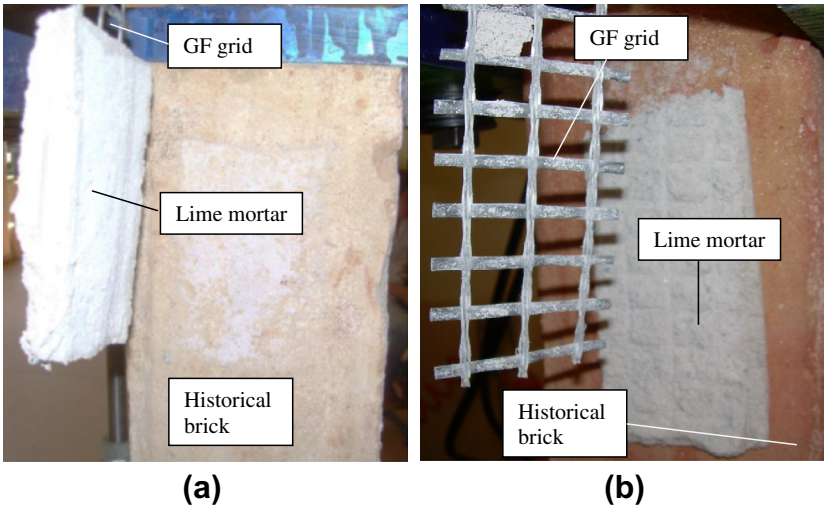

Fig. 7. GF grid and lime based mortar. Experimental failure modes for anchorage lengths (a) of 100 mm, debonding of mortar–GF grid system from the support and (b) 150 mm, debonding of the grid from mortar.

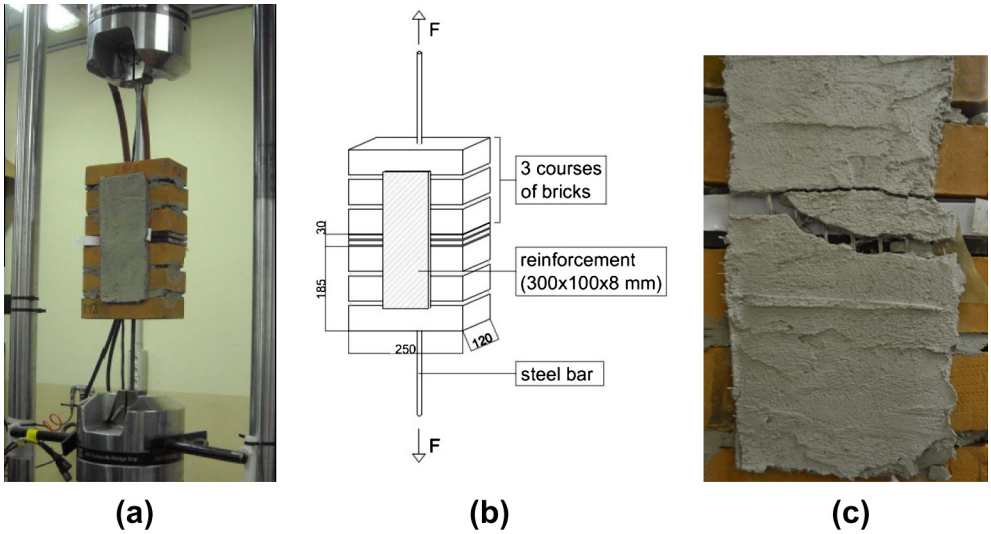

Fig. 8. Experimental set-up for debonding tests on masonry pillars. (a) The specimens during a test, (b) geometry of the specimens, and (c) detail of a reinforcement failure.

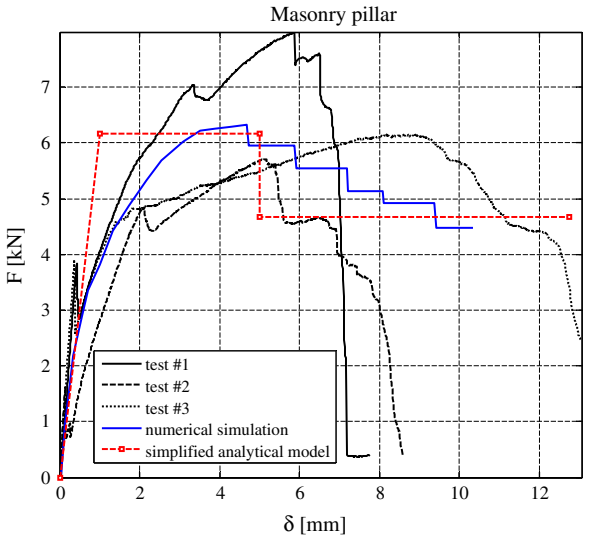

Fig. 9. Small pillar. Experimental force–displacement curves compared to numerical predictions and simplified model.

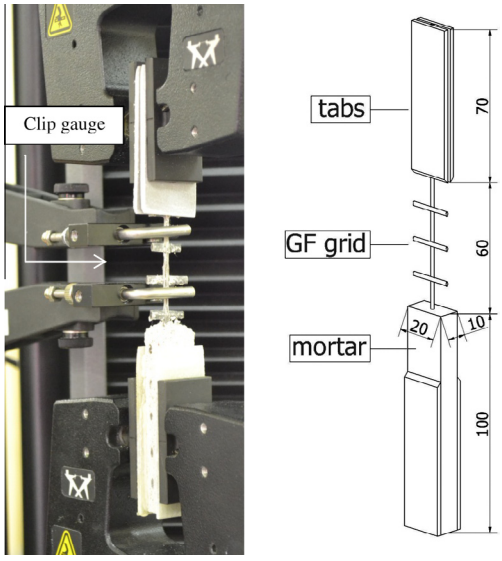

Fig. 10. Specimen to determine the mortar–GF grid interface behavior: (A) during testing and (B) specimen geometry (dimensions in mm).

3. Simplified model for FRCM composites

A simplified analytical assessment is proposed in this section, assuming that all the deformability and the failure mechanism occurs in the system constituted by the grid and the mortar.

Within the simplified model proposed, the following assumptions are made:

(1) A mechanism composed by two non-linear springs disposed in series and constituted by the unbounded and bonded grid. The total deformation of the system is therefore due to the sum of the axial deformation of the unbounded GFRP grid and the contribution of the pure sliding of the grid within the surrounding mortar. For the sake of simplicity, it is assumed that the yarn undergoes axial deformation only in the unbounded region. Its length is reasonably assumed equal to L_u = 150 mm. The number of yarns is indicated with the symbol n_y.

(2) An elastic perfectly plastic behavior of the interface between grid and mortar, exhibiting an idealized stepped stress–slip behavior as in Fig. 11. In Fig. 11, k_t indicates the elastic tangential stiffness of the yarn–mortar interface, whereas c_I and c_{II} the peak and residual strength. The bonded region is indicated with the symbol L_b.

(3) An elastic–perfectly plastic behavior with infinite ductility of the FRP yarn, see Fig. 12, having elastic stiffness equal to $k_n = E_{FRP}A_{FRP}$ and ultimate strength equal to $F_u = f_{u\text{-}FRP}A_{FRP}$, where E_{FRP} = 70000 MPa is the yarn modulus, $f_{u\text{-}FRP}$ = 1200 - MPa is the yarn ultimate strength and A_{FRP} is the transversal area of the single yarn.

The transversal area of the single yarn may be evaluated experimentally, once $f_{u\text{-}FRP}$ is known, from direct tensile tests performed on a single yarn and conducted within the present research. It is worth noting that, while the behavior of the GF is brittle, i.e. the transmitted tensile stress vanishes when the rupture strength $f_{u\text{-}FRP}$ is reached, little differences

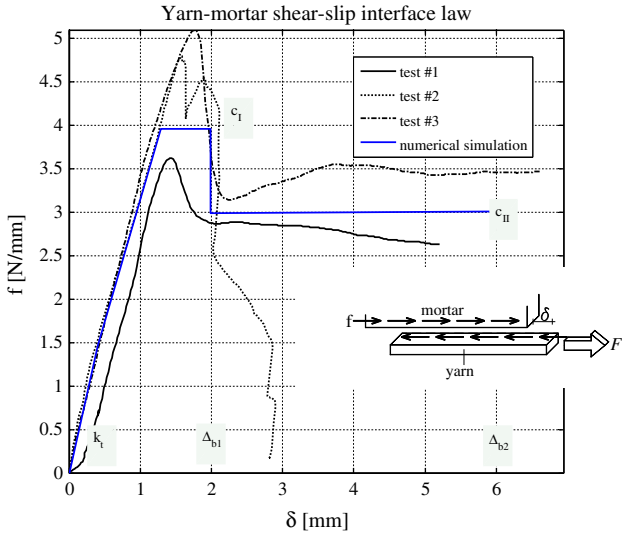

Fig. 11. experimental tangential stress–slip behavior of the GF yarn–mortar interface. In the figure, c_I and c_{II} are ultimate interface force values, with corresponding slip values equal to Δ_{b1} and Δ_{b2}. k_t is the elastic stiffness value.

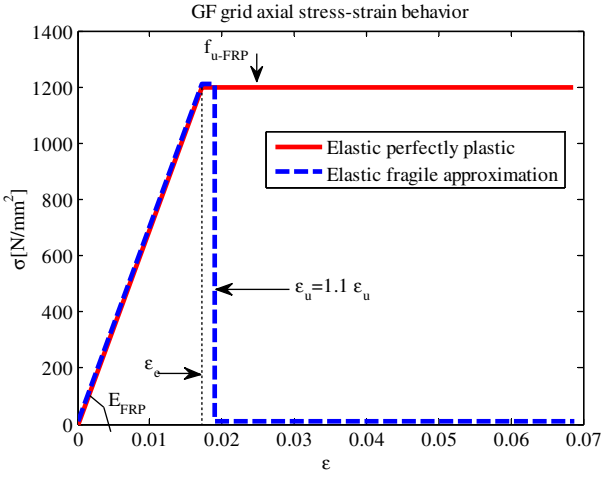

Fig. 12. Hypotheses assumed for the axial stress–strain diagrams of the GF yarns in the numerical models: elastic perfectly plastic model and elastic fragile approximation.

occur assuming either an elastic–perfectly plastic or damaging behavior for the yarns. Indeed, rupture of the yarn is experienced experimentally only for an anchorage length equal to 150 mm, whereas in all the other cases GF grid tensile stress remains under the elastic limit. For the specimen with anchorage length equal to 150 mm, only one external yarn breaks, and this physical evidence is reproduced numerically adding a small eccentricity of the external applied load. In this latter case, the only difference between the assumption of an elastic–perfectly plastic and a brittle behavior for GF grid is that, when $f_{u\text{-}FRP}$ is reached in one yarn, in the first case the mechanical system fails (i.e. a mechanism activates) with external force applied equal to the peak load, whereas in the second the same failure mechanism occurs, but with an external force vanishing. Let us indicate with F the external load applied, with F_i the forces acting on the ith yarn, with e the external load eccentricity and with L the distance between two contiguous yarns. Translational and rotational equilibrium equations require that:

$$\begin{aligned} F &= F_1 + F_2 + F_3 \\ Fe &= F_1 L - F_3 L \end{aligned} \tag{1}$$

Compatibility conditions for the yarns, assuming an elastic behavior read:

$$\begin{aligned} u_i &= \Delta L_u \frac{F_i}{A_{FRP} E_{FRP}} \\ u_1 - u_3 &= 2\vartheta L \\ u &= u_2 = \frac{u_1 + u_3}{2} \end{aligned} \tag{2}$$

where u_i is the displacement of the ith yarn in correspondence of its extreme free to translate, ΔL_u is the unbounded part of the grid and ϑ is the rotation of the rigid part connecting perpendicularly the three yarns in correspondence of their extremes free to translate. Equation system (1) + (2) is a 7 equations system with 7 unknowns (u_i, F_i and ϑ) which may be solved at increasing values of the external load F.

From Eq. (1), it appears evident that, when one of the yarns, say the first, reaches an ultimate strength equal to $F_u = f_{u\text{-}FRP} A_{FRP}$, the system is univocally determined, so that $F_3 = -Fe/L + F_u$ and $F_2 = F\left(1 + \frac{e}{L}\right) - 2F_u$. In presence of an elastic–perfectly plastic material, an increase of the external load is still possible until $F_2 = F_u$. In this latter case, the specimen fails, with $F_3 = -Fe/L + F_u$ and with a failure load equal to $3F_u - Fe/L$. Conversely, when a brittle behavior is assumed for the yarn, immediately after that the first yarns reaches its limit strength, the second Eq. (1) would require a negative external load $F = -F_3 L/e$, which is clearly impossible considering also that yarns are assumed unable to withstand compressive stresses.

(4) As it can be easily shown, for the mechanical system constituted by the three yarns disposed in parallel in presence of load eccentricity, when one of the three yarns fails and the material is brittle (F_1=0), equilibrium is still possible only if F drops to zero.

(5) A negligible deformation of the brick and masonry pillar, which appears reasonable considering that cracks occur almost exclusively in the mortar.

By means of the aforementioned hypotheses, it can be easily shown that the stiffness of the mechanical system constituted by the unbounded and bonded part is:

$$K_T = (L_u + L_b)\left(\frac{E_{FRP} n_y A_{FRP}}{L_u} + n_y k_t\right)\frac{\Delta L_u + \Delta L_b}{L_u + L_b} \tag{3}$$

where ΔL_u is the overall displacement due to the unbounded part and ΔL_b is the overall displacement of the bonded part.

The peak load is evaluated as follows (if larger values for the ultimate load associated to tensile failure of the grid are obtained):

$$F_{u1} = n_y c_I L_b \tag{4}$$

The displacement value at the elastic limit is:

$$\Delta s_e = F_{u1}\frac{L_u + L_b}{K_T} \tag{5}$$

The displacement value reached when the tangential force at the interface between yarn and mortar shifts from peak to residual value is the following:

$$\Delta s_{u1} = \Delta L_{u1} + \Delta_{b1} \tag{6}$$

Where $\Delta L_{u1} = F_{u1} L_u / (E_{FRP} n_y A_{FRP})$ and Δ_{b1} is defined in Fig. 11 and corresponds to a slip where the interface strength drops from the peak to the residual load.

Similarly, the residual strength of the overall system is evaluated as:

$$F_{u2} = n_y c_{II} L_b \tag{7}$$

The displacement value reached in correspondence of a drop of the tangential force from the residual value to zero is:

$$\Delta s_{u2} = \Delta L_{u2} + \Delta_{b2} \tag{8}$$

where $\Delta L_{u2} = F_{u2} L_u / (E_{FRP} n_y A_{FRP})$ and Δ_{b2}, see Fig. 11, corresponds to a slip where the interface strength drops from the residual load to zero.

Conversely, if the failure is associated to an axial stress in a yarn reaching the ultimate value $f_{u\text{-FRP}}$, then the failure load is:

$$F_u = n_y A_{FRP} f_{u\text{-FRP}} \tag{9}$$

Authors experienced that, both numerically and experimentally, this last situation never occurs, i.e. failure is due to sliding of the bonded part of the grid.

As it is possible to note from the force–displacement curves reported in Figs. 3–5 for anchorage lengths respectively equal to 50, 100 and 150 mm, and where the response obtained using the simplified analytical model proposed in this section is also represented and indicated with the label "simplified analytical model", very accurate predictions of both deformability and strength of the specimens is obtained.

In order to reproduce the actual experimental behavior of the reinforced specimen having an anchorage length equal to 150 mm, where a tensile failure of one of the yarns is experienced, an elasto-plastic FE beam analysis as in Fig. 13 is performed. Only the grid is modeled by means of beam elements. When dealing with the part of the grid embedded in the mortar, two different typologies of elements are utilized, hereafter called A1 and A2, depending if they are part of a yarn or of the transversal grid respectively. When dealing with an element belonging to a longitudinal yarn (A1), each element is kinematically characterized by the longitudinal displacement field u. From longitudinal equilibrium equation involving FRP tensile stress σ and tangential actions τ due to sliding between yarn and surrounding mortar, the following differential equation may be written:

$$\frac{d\sigma}{dx} = \tau \frac{A_L}{A_{FRP}} = \tau \xi \tag{10}$$

where A_L is the perimeter of the yarn and A_{FRP} is the transversal area of a single yarn (hereafter assumed equal to 0.9 mm^2) and $\frac{A_L}{A_{FRP}} = \xi$.

From Hooke's law of the yarn and imposing an elastic relationship between tangential actions and yarn/mortar slip, it is also possible to write the following relations:

$$\begin{aligned} \sigma &= E_{FRP} \frac{du}{dx} \\ \tau &= k_t u \end{aligned} \tag{11}$$

where k_t is the yarn/mortar interface elastic shear modulus, that can be deduced from the experimental stress–slip relation depicted in Fig. 11.

From Eqs. (10) and (11), we obtain the following second order differential equation for the axial displacement field of the yarn:

$$\frac{d^2 u}{dx^2} - u \frac{k_t}{E_{FRP}} \xi = 0 \tag{12}$$

Each element belonging to longitudinal yarns obeys Eq. (12), therefore the (exact) interpolation of the displacement field adopted is the following:

$$u(x) = A_0 e^{-\lambda x} + B_0 e^{\lambda x} \tag{13}$$

Having indicated with $\lambda = \sqrt{\xi k_t / E_{FRP}}$.

Eq. (13) may be re-written in terms of end nodes displacements u_2 and u_3 (see Fig. 13) as:

$$u(x) = \frac{u_2 - u_3 e^{\lambda L_{2\text{-}3}}}{e^{-\lambda L_{2\text{-}3}} - e^{\lambda L_{2\text{-}3}}} e^{-\lambda x} + \frac{u_3 e^{-\lambda L_{2\text{-}3}} - u_2}{e^{-\lambda L_{2\text{-}3}} - e^{\lambda L_{2\text{-}3}}} e^{\lambda x} \tag{14}$$

When dealing with elements belonging to the transversal yarns, a common Winkler element is utilized with rotational end releases, Fig. 13.

A linear elastic software (developed in Matlab environment) is utilized to reproduce the experimental behavior of the specimen. Since it was found experimentally that only 1 yarn per glued grid collapses when it reaches an ultimate tensile stress equal to $f_{u\text{-FRP}}$, a small eccentricity e was applied to the end section force, Fig. 13, in order to simulate an experimental imperfection that can cause a rigid rotation of the end section where the external force is applied. The exact value adopted for e in the simulations can be found by means of an iterative trial and error strategy where the objective is to equate the maximum tensile stress reached in one of the yarns to the ultimate stress of the fiber. It is found that $f_{u\text{-FRP}}$ is reached in one of the external yarns for a force acting of about 4 kN (approximately equal to the experimental failure load applied to the specimen, see Fig. 5) with an eccentricity equal to 1.98 mm.

In Fig. 14a, the deformed shape of the FE model with F = 3.5 kN is represented, with the corresponding value of distribution of tangential actions on yarns–mortar interface tangential stress (Fig. 14b) and yarns tensile stresses Fig. 14c. Values are normalized with the ultimate strength values, so that values lower than 1 indicate that the interface (or the yarn) are in the elastic regime.

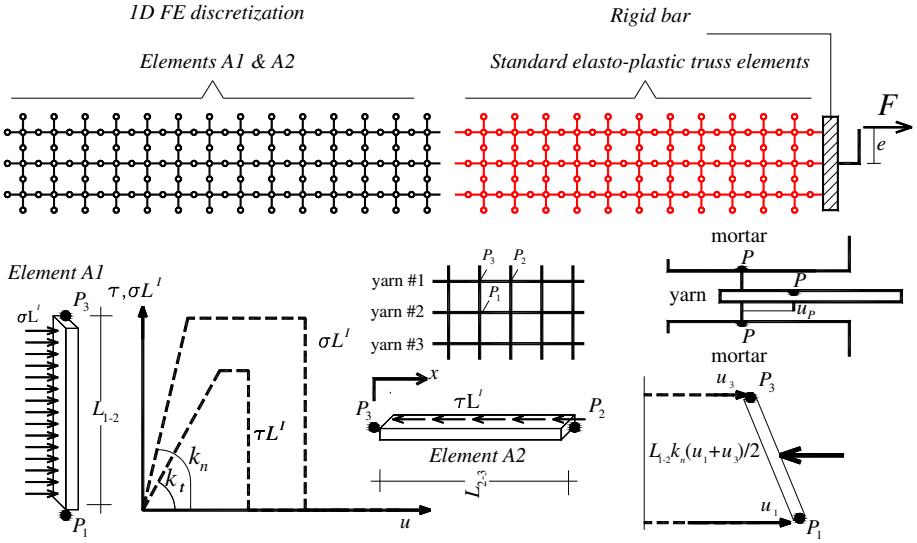

Fig. 13. FE beam element utilized for the simplified elasto-plastic computation of the grid.

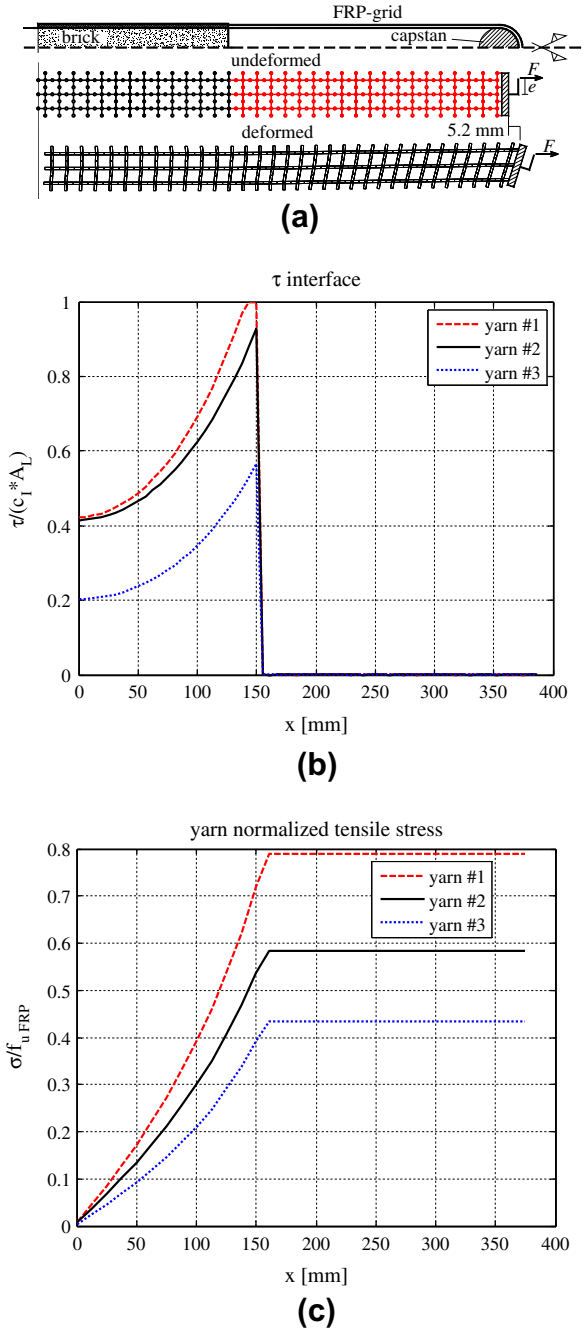

Fig. 14. Elastic results at $F = 3.5$ kN. (a) Deformed shape of the fabric strip, (b) normalized tangential action on the yarns ($\tau/(c_I/A_L)$): values lower than 1 indicate that yarn–mortar interface is in the elastic regime, and (c) normal stress acting in the yarns.

The value of the external load selected corresponds to the first plasticization of yarn #1–mortar interfaces, near the boundary of the brick, as can be easily noticed from the normalized plot of tangential stresses represented in Fig. 14b. In addition, from Fig. 14c, it can be noted that all wires exhibit values of tensile stress lower that the maximum allowable, meaning that they are still in elastic phase.

When the load is increased up to 4 kN, which corresponds to the failure of yarn #1 for a tensile stress reaching $f_{u\text{-FRP}}$, the tangential actions increase on all yarns, undergoing diffused plasticization for yarn #1, see Fig. 15a. A plasticization of the interface in its initial stage may be also noted for the second yarn. Normalized tensile

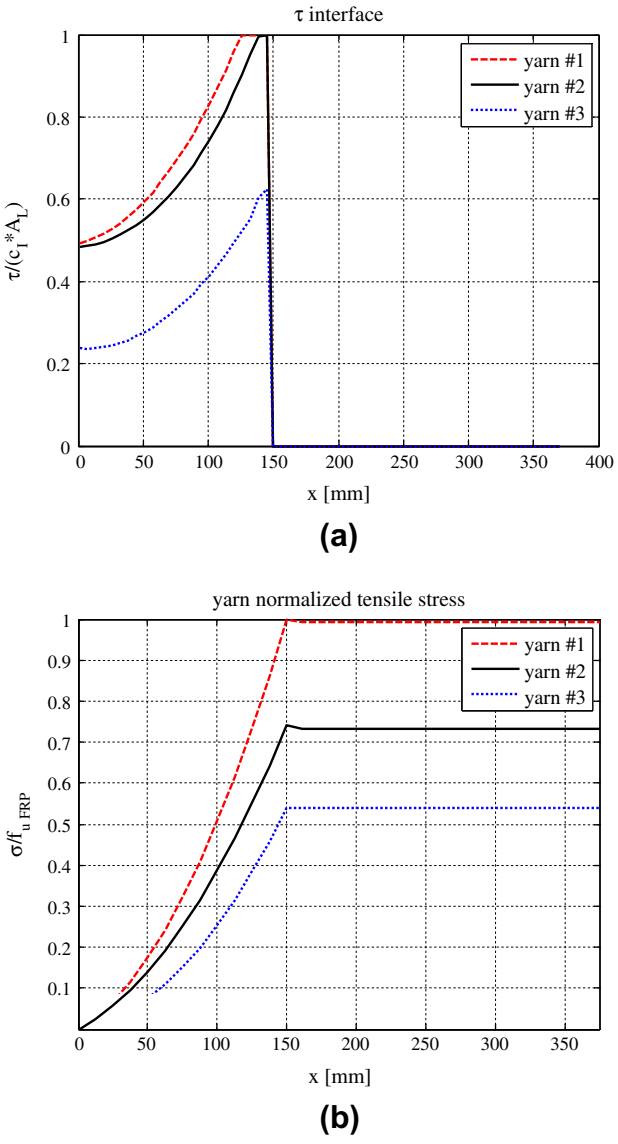

Fig. 15. Results near collapse ($F = 4.0$ kN). (a) Normalized tangential action on the wire ($\tau/(c_I/A_L)$): values lower than 1 indicate that wire–mortar interface is in the elastic regime. (b) Normal stress acting on the wire.

stresses are finally represented in Fig. 15b, where it is clearly shown that yarn #1 reaches its ultimate resistance value.

The load displacement curve found with the 1D FE model is finally compared with experimental evidences in Fig. 5, again exhibiting a satisfactory agreement and a quasi linear behavior up to the tensile failure of one of the yarns (the slight deviation from linearity is obviously associated to the diffusion of plasticization inside the GF grid –mortar interface).

4. Full 3D-FEM non-linear approach

The non-linear FEM approach adopted in this paper and used to fit previously discussed experimental data is basically an extension of the procedure originally adopted in Milani and Lourenço [21] and, before but with different FEs, in Milani and Tralli [22].

The FE model is constituted by a discretization with 3D rigid and infinitely resistant eight-noded elements. Between continuous elements, quadrilateral non-linear interfaces are present.

Because of the fact that elements are rigid and infinitely resistant, all deformation (linear and non-linear) is lumped on

interfaces. In this way, a reduction of the optimization variables is obtained.

Kinematic variables are centroid displacements $\left(u_x^E, u_y^E, u_z^E\right)$ and rotations around the centroid $\left(\Phi_x^E, \Phi_y^E, \Phi_z^E\right)$, see Fig. 16. Jump of displacements on interfaces is linear.

To further simplify the calculations, three translational and three rotational non-linear springs are utilized for each interface, Fig. 16. As well known, for brittle materials bending behavior of the interfaces may have a dependence on in-plane compression and such feature is taken into account in the code by means of the approximate procedure described in detail in [21,22], where the reader is referred to for further details.

A Sequential Quadratic Programming scheme – SQP – is utilized to deal with softening, approximating the actual stress–strain behavior of the interfaces by means of a stepping function with a priori fixed accuracy, as depicted in Fig. 17, where the stress–strain behaviors in tension and compression adopted in the present research to model the bricks and the mortar are represented.

The utilization of quadratic programming to deal with elasto-plastic materials was first proposed in [25,26] and appears nowadays quite interesting in light of the improvements in the field of mathematical programming algorithms, obtained in the last few years thanks also to the utilization of computers with increased RAM. The sequential scheme is necessary when softening (or limited ductility) of the materials is present and was first proposed in [22].

The stress–strain behavior of each interface is deduced either from proper mechanical characterization or preliminary numerical procedures. The relationship between continuum strains ε_n and an interface displacement is deduced by means of well-established averaging procedures, as pointed out in [27] by Kawai. The stress–strain relationship is therefore known for each point of the interface.

Being the model constituted by 6 elastic–plastic springs, Fig. 16, and assuming that at each iteration the interfaces behave as they were elastic–perfectly plastic, only 12 plastic multipliers for interface (two for each spring, λ^+ and λ^-, one for a positive and one for a negative displacement) add to the total optimization variables. To summarize, optimization variables are the following: 12 plastic multipliers for interface and 6 generalized displacements (including rotations) per element.

In this framework, to achieve a step by step solution of the discretized elasto-plastic problem, the following Quadratic Programming – QP – has to be solved at each iteration, see [21,22] – [25,26]:

$$\begin{cases} \min & \left\{\frac{1}{2}[(\Delta\boldsymbol{\lambda}^+ - \Delta\boldsymbol{\lambda}^-)^T \mathbf{K}_{ep}(\Delta\boldsymbol{\lambda}^+ - \Delta\boldsymbol{\lambda}^-) \right. \\ & \left. + \Delta\mathbf{U}_{el}^T \mathbf{K}_{el} \Delta\mathbf{U}_{el}] - \Delta\mathbf{F}^T \Delta\mathbf{U}_{el} \right. \\ \text{subject to :} & \Delta\boldsymbol{\lambda}^+ \geqslant \mathbf{0}\ \Delta\boldsymbol{\lambda}^- \geqslant \mathbf{0} \end{cases} \tag{15}$$

In Eq. (15) $\mathbf{K}_{el}$ represents the $6n_{el} \times 6n_{el}$ assembled elastic stiffness matrix, where n_{el} is the number of elements, $\Delta\boldsymbol{\lambda}^+$ and $\Delta\boldsymbol{\lambda}^-$ are two $12n_{in}$ vectors of the plastic multiplier increments of each non-linear spring (e.g. flexure, shear, etc.), where n_{in} is the number of interfaces, $\mathbf{K}_{ep}$ is a diagonal $12n_{in} \times 12n_{in}$ matrix collecting interfaces hardening moduli, $\Delta\mathbf{U}_{el}$ is a $6n_{el}$ vector of elements displacement and rotation increments, $\Delta\mathbf{F}$ is the $6n_{el}$ vector of external loads increments.

A detailed description of the features of the SQP scheme adopted is provided in [22] and is not repeated here for the sake

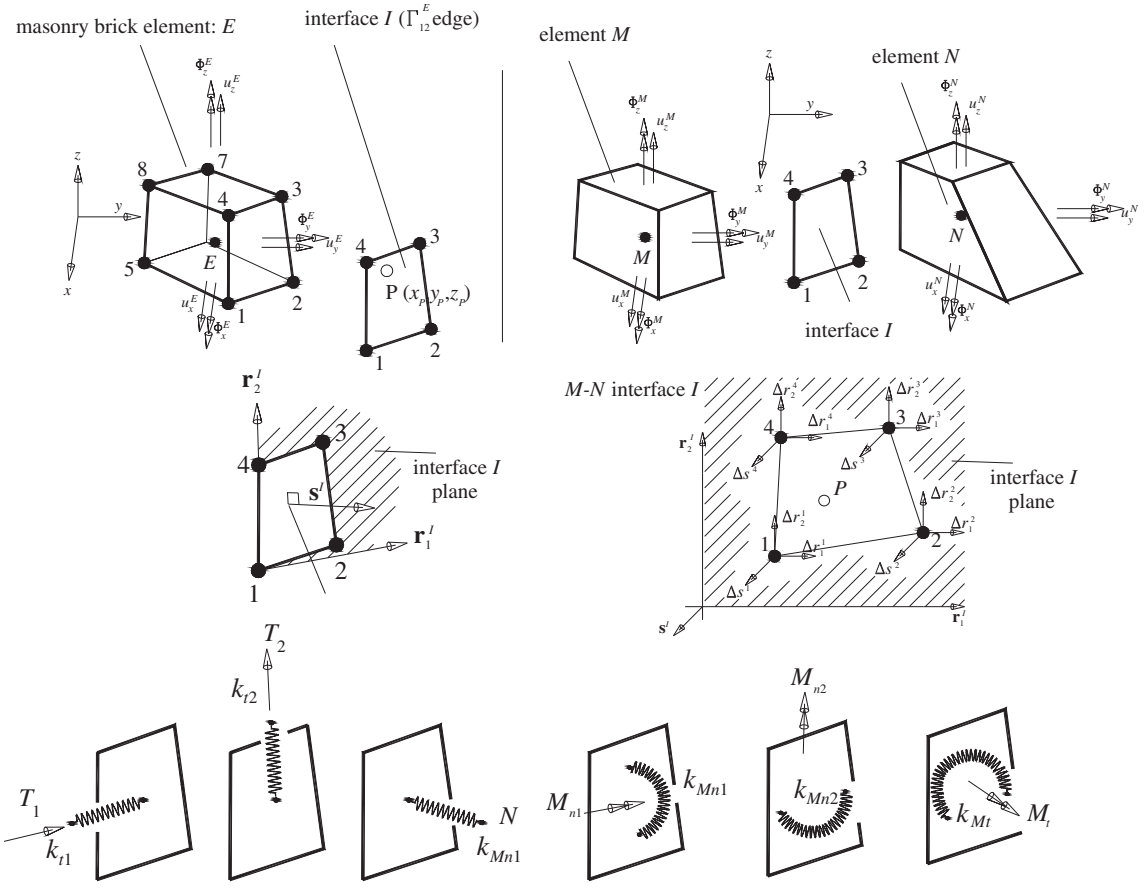

Fig. 16. Rigid infinitely resistant eight-noded parallelepiped element used for bridges 3D discretization and kinematics of interfaces between contiguous elements.

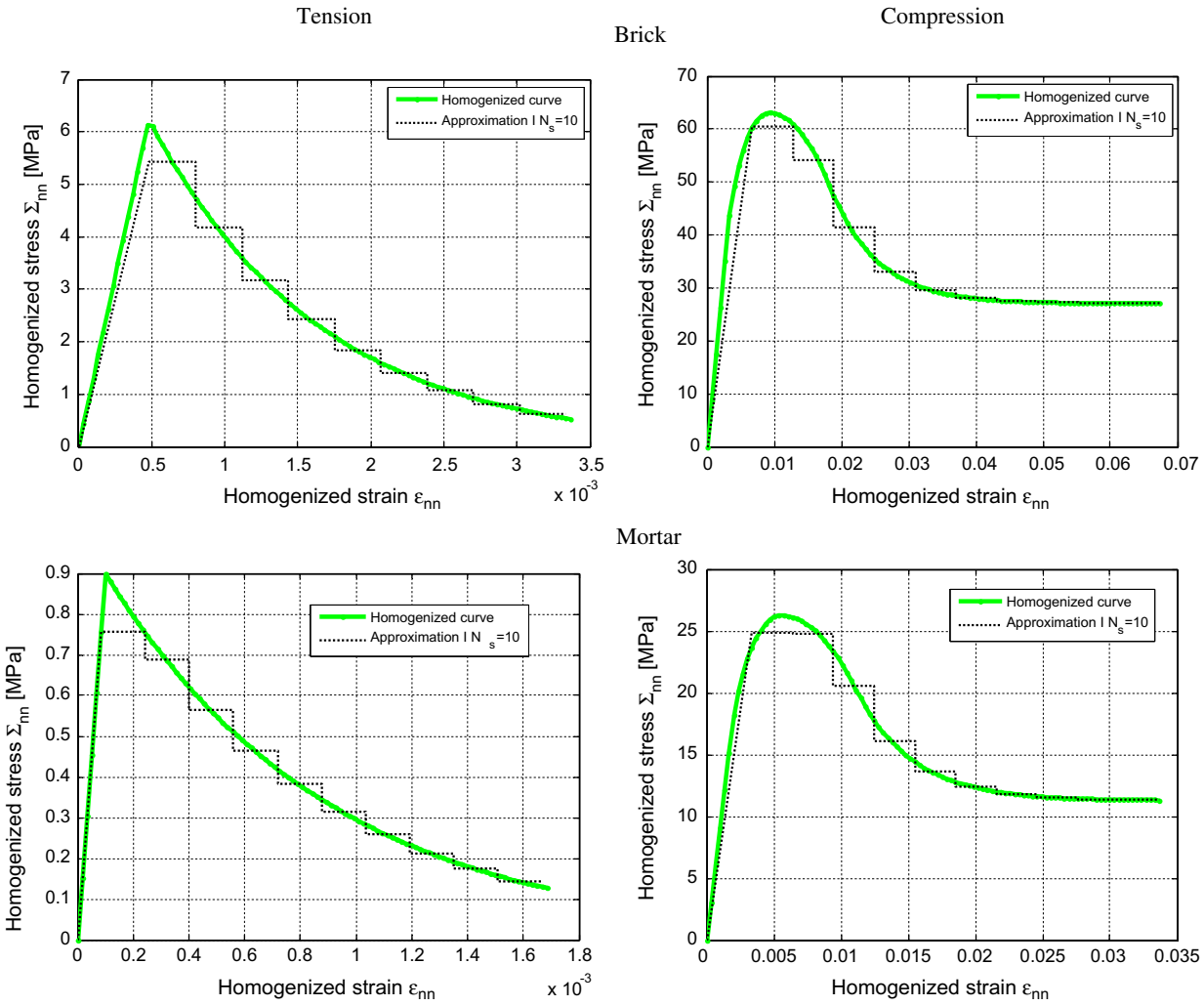

Fig. 17. Numerical uniaxial stress–strain relationships in tension and compression used for bricks and mortar.

of conciseness. However it is worth noting that the trial-and-error step-length sizing strategy discussed above is generally quite efficient but may become particularly burdensome in presence of models with many interfaces and/or when the linear piecewise constant approximation assumed for the interface springs is very refined. This is an intrinsic limitation of the proposed procedure. For these reasons, crude approximations of the non-linear behavior of the springs are used.

4.1. FRP grid modeling: truss and 1D interface elements

A meaningful extension of the previously presented numerical model was necessary to properly take into account the presence of the GF grid, and especially the non-linear interfacial behavior between single yearns and surrounding mortar material.

In particular, a single yarn, identified geometrically by the unitary vector **t** parallel to the longitudinal direction of the yarn is modeled by means of rigid infinitely resistant truss elements, as schematically shown in Fig. 18. This hypothesis is acceptable since the elastic modulus and the ultimate strength of the fibers are much higher than in the mortar (at least two orders of magnitude). Each element is therefore associated to 6 kinematic variables, namely three centroid displacements $\mathbf{u}^E = \left(u_x^E, u_y^E, u_z^E\right)$ and three rotations around centroid G $\mathbf{\Phi}^E = \left(\Phi_x^E, \Phi_y^E, \Phi_z^E\right)$. Contiguous truss elements are interconnected by a translational axial spring disposed parallel to **t**, whereas jumps of displacement along tangential directions are not allowed. Furthermore, rotation of the elements with axis parallel to **t** direction is set equal to zero.

The axial behavior of the yarn is assumed elastic perfectly plastic, as shown schematically in Fig. 18, with ultimate strength corresponding to that of the GF grid.

The tangential stress–sliding relationship between the yarn and surrounding mortar is assumed as in Fig. 11. Let us consider a truss element E and four parallelepiped elements of the surrounding mortar M, N, T and Q. Due to the rigid element kinematic assumed, the slip function along a single truss element is linear. It is therefore sufficient to evaluate slip on the extreme nodes P_1 and P_2. Focusing on P_1 (the same considerations may be repeated for P_2), the absolute displacement along **t** of element E is u_t^{E1}. u_t^{E1} may be easily evaluated when $\mathbf{u}^E$ and $\mathbf{\Phi}^E$ vectors are known. The same considerations hold for elements M, N, T and Q, so that u_t^{M1}, u_t^{N1}, u_t^{T1} and u_t^{Q1} represent the displacement of each surrounding element (with obvious meaning of the superscripts) along **t** direction in correspondence of node P_1.

The relative tangential slip may be therefore evaluated as follows:

$$\Delta s^{P1} = u_t^{E1} - \frac{u_t^{M1} + u_t^{N1} + u_t^{T1} + u_t^{Q1}}{4} \tag{16}$$

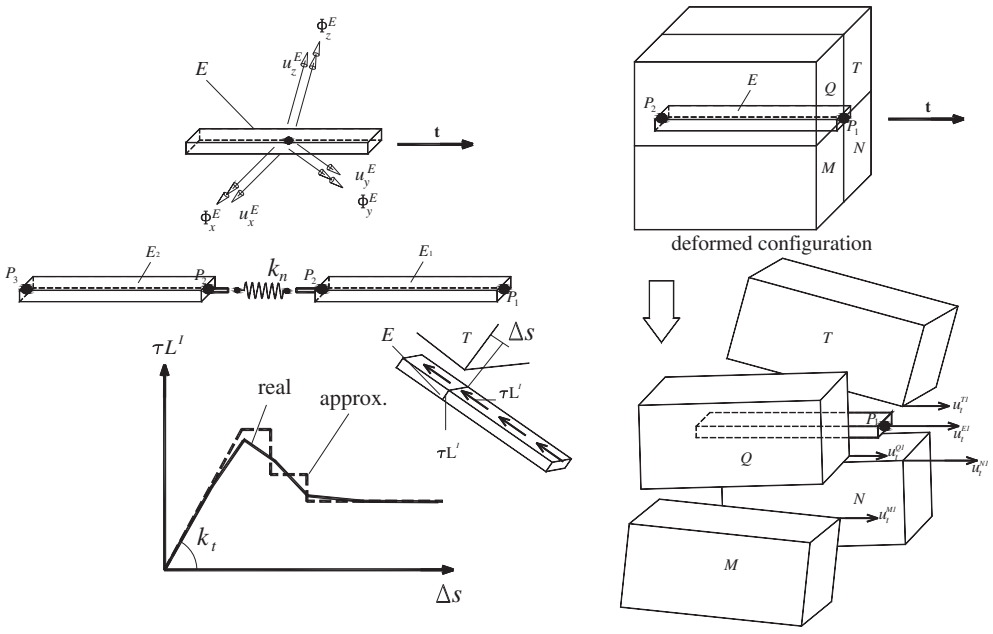

Fig. 18. Schematization of the GF grid (left) and of the interaction between grid and mortar (right).

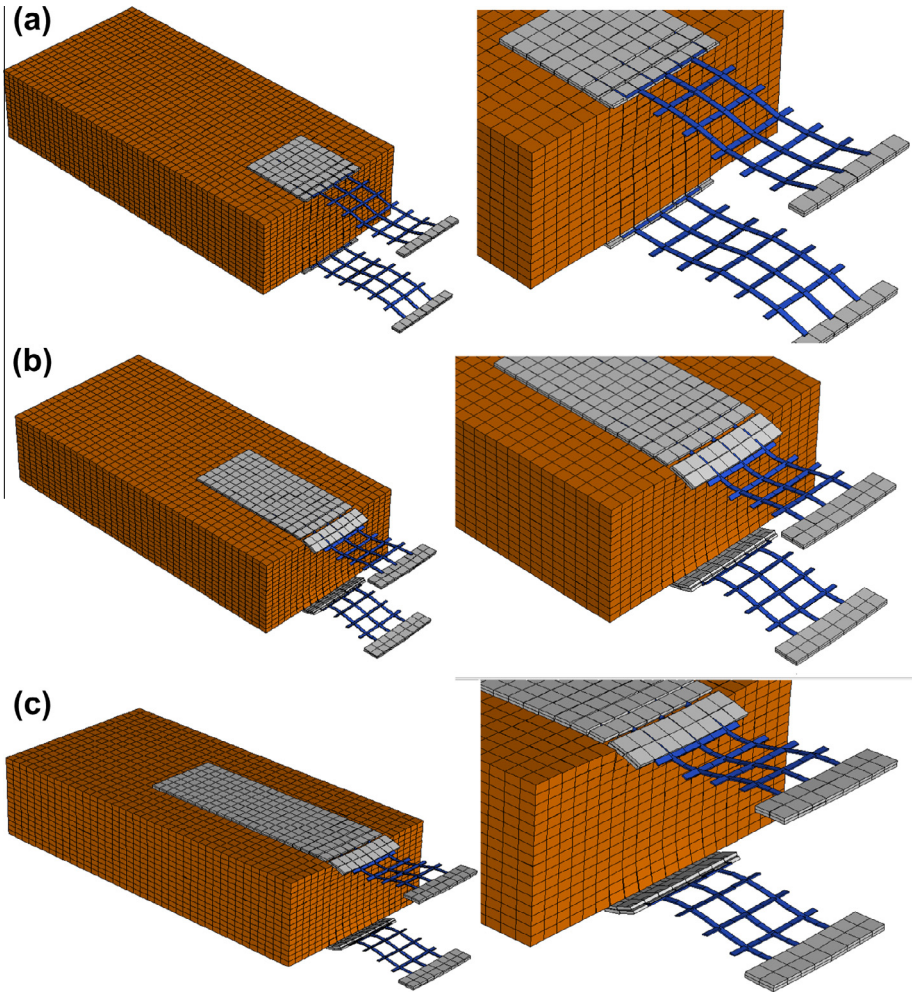

Fig. 19. Single brick reinforcement. Deformed shapes at peak provided by the non-linear FE code. (a) 50 mm anchorage, (b) 100 mm anchorage, and (c) 150 mm anchorage.

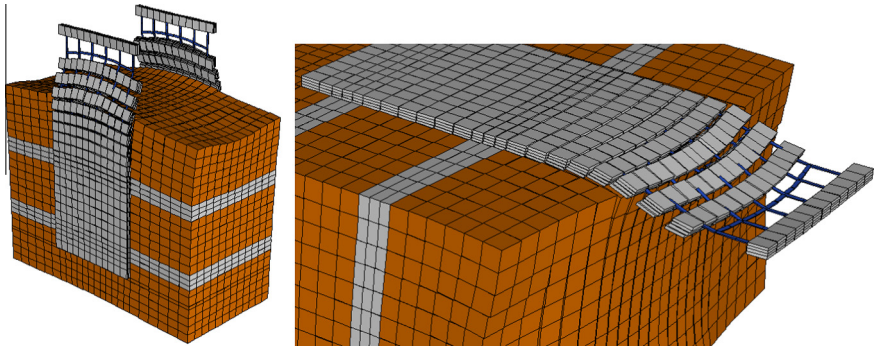

Fig. 20. Masonry pillar reinforcement. Deformed shapes at peak provided by the non-linear FE code.

The numerical relationship of the interface utilized is again idealized by means of a stepping constant function, see Fig. 11, so that (15) may be again used to predict the non-linear behavior of the reinforced specimens by means of mathematical programming.

5. Comparison between experimental and numerical results

The load–displacement curves obtained by means of the aforementioned numerical approach are compared with the experimental data in Figs. 3–5 for the single brick reinforcement system (anchorage lengths respectively equal to 50, 100 and 150 mm), whereas numerical results for the masonry pillar are compared with experimental data in Fig. 9.

As can be noted, a very promising agreement is found in the evaluation of the peak load, initial undamaged state stiffness and post-peak behavior.

Deformed shapes near failure obtained numerically are depicted respectively in Figs. 19 and 20 for the reinforced single brick and the masonry pillar, respectively. In all the produced simulations a debonding of the GF grid within mortar was detected. As it can be noted, the agreement with experimental results is very promising, exception made for the failure mechanism of the specimen with anchorage length equal to 150 mm, Fig. 19c. In this latter case, indeed, tensile failure of one yarn was experimentally experienced. The failure mechanism is not symmetric, meaning that an accidental experimental imperfection causing a rotation of the loaded pad, associated to different tensile stresses acting on the yarns, was present. As it was shown in the previous section within the simplified analytical–numerical model, the presence of a lateral eccentricity of the applied load results into both a rotation of the pad where the load is applied and an increase of the tensile stress in one of the lateral yarns. The overload acting on one yarn causes its premature rupture and is associated to the asymmetric failure mechanisms observed experimentally. Authors experienced the same behavior within the present numerical model applying an eccentricity of the load equal to those calculated in the simplified analytical–numerical model discussed in the previous section.

To further assess FE results, a sensitivity analysis on the brick reinforced with the fabric exhibiting anchorage length equal to 150 mm is conducted by means of both the 1D and the full 3D FE model, varying load eccentricity in a wide range and assuming for the yarns, see Fig. 12, either an elastic–perfectly plastic behavior with infinite ductility or an elastic–perfectly plastic model where the resistance of the yarn vanishes after an axial deformation $\varepsilon_u = 1.1\varepsilon_e$, is reached being $\varepsilon_e = f_{u\text{-FRP}}/E_{FRP}$ the elastic limit deformation. This latter hypothesis approximates better the actual behavior of a GF yarn.

Assuming as eccentricity $e_0 = 1.98$ mm that was considered to fit experimental data, numerical simulations are repeated with eccentricities $e = 0$, $1/2e_0$, and $2e_0$ respectively. Results in terms of global load–displacement curves are summarized in Fig. 21a. As can be noticed, 1D and full 3D models provide very similar results. In addition, it is interesting to highlight that rupture of the

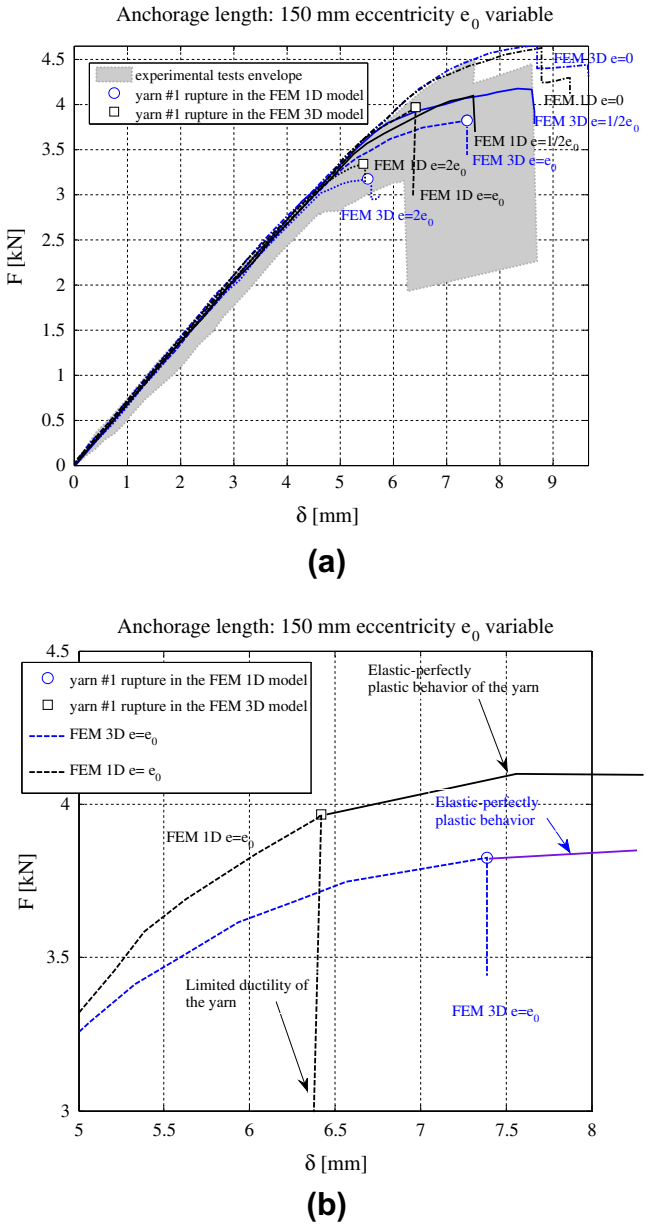

Fig. 21. Reinforced brick, anchorage length equal to 150 mm. (a) Sensitivity analysis varying load eccentricity. (b) Detail of the behavior of a model with infinite or very deduced ductility of the yarns.

yarn is always experienced with eccentricities greater than $1/2e_0$. Varying the eccentricity between $1/2e_0$ and e_0 by means of a standard bisectional procedure, the authors found that the eccentricities activating yarn #1 rupture are equal to $0.91e_0$ and $0.85e_0$ for the 1D and full 3D model respectively. The difference in assuming an elastic–perfectly plastic behavior or a model with reduced ductility ($\varepsilon_u = 1.1\varepsilon_e$) for the yarns is minimal, as can be observed in the detail in Fig. 21b, where the behavior near failure of both models is compared for an eccentricity equal to $2e_0$. This is obviously due to the equilibrium constrains to be imposed in the yarns system, Eq. (1), which results into an evaluation of very similar peak loads. The only remarkable difference is connected to the overall ductility of the system, which is obviously infinite for a model where materials exhibit infinite ductility.

6. Conclusions

The paper analyzed the behavior of single bricks and small masonry pillars strengthened by means of fabric reinforced cementitious matrix systems made with GF grids both from an experimental and numerical standpoint.

The experimental activities included:

- The characterization of the constituent materials (GF grid, mortar and bricks).
- A series of tests on single bricks with a double reinforcements on two opposite sides.
- A series of small pillars of bricks again with double reinforcements.

The experimental results showed that the ultimate strength depends on the bonded surface and on the type of mortar.

Two complementary numerical tools were presented to simulate the experiments. In the first model, based on an analytical–numerical approach, only the FRCM composite is considered and modeled by means of 1D Finite Elements interacting with the surrounding mortar by means of interfaces exhibiting a non-linear stress–slip behavior deduced from experimental data.

The second model is a fully 3D Finite Element approach, based on Sequential Quadratic Programming and uses 8-noded rigid elements interconnected by inelastic interfaces exhibiting softening. The GF grid reinforcement is modeled through non-linear truss elements, interacting with surrounding mortar by means of non-linear interfacial tangential stresses.

Both models were able to fully simulate the experimental evidences, exception made for the reinforced double lap single brick with anchorage length equal to 150 mm. In this case, a tensile failure of the single yarns is experienced, which it is shown by the analytical–numerical model to be a consequence of a small unavoidable eccentricity of the load during the experiment. As a conclusive remark, it can be stated that the proposed combined approaches may be considered as references for design considerations.

Acknowledgement

These tests were performed on specimens produced using reinforcing materials and mortars distributed by Sika Italia. Their financial support is gratefully acknowledged.

References

[1] Corradi M, Borri A, Vignoli A. Strengthening techniques tested on masonry structures struck by the Umbria–Marche earthquake of 1997–1998. Constr Build Mater 2002;16:229–39.
[2] Milani G, Milani E, Tralli A. Approximate limit analysis of full scale FRP-reinforced masonry buildings through a 3D homogenized FE package. Compos Struct 2010;92:918–35.
[3] Ghiassi B, Marcari G, Oliveira DV, Lourenço PB. Numerical analysis of bond behavior between masonry bricks and composite materials. Eng Struct 2012;43:210–20.
[4] Schwegler G. Masonry construction strengthened with composites in seismically endangered zone. In: Proc 10th European conference on earthquake engineering; 1994. p. 2299–303.
[5] Eshani MR. Strengthening of earthquake damaged masonry structures with composite materials. In Proc nonmetallic (FRP) reinforcement for concrete structures. Proceedings of the second international RILEM, symposium FRPRCS-2; 1997. p. 681–7.
[6] Saadmantesh H. Fiber composites of new and existing structures. ACI Struct J 1991;91(3):346–54.
[7] Triantafillou TC. Composites: a new possibility for the shear strengthening of concrete, masonry and wood. Compos Sci Technol 1998;58:1285–95.
[8] Triantafillou TC. A new generation of composite materials as alternative to fiber reinforced polymers for strengthening and seismic retrofitting of structures. In: Nicolais L, Meo M, Milella E, editors, Proc composite materials. A vision for the future. Springer-Verlag London Limited; 2011.
[9] De Caso Y, Basalo FJ, Matta F, Nanni A. Fiber reinforced cement-based composite system for concrete confinement. Constr Build Mater 2012;32:55–65.
[10] Nanni A. FRCM strengthening – a new tool in the concrete and masonry repair toolbox. Concr Int Des Constr 2012;34(4):43–9.
[11] D'Ambrisi A, Feo L, Focacci F. Experimental analysis on bond between PBO-FRCM strengthening materials and concrete. Compos B Eng 2012;44(1):524–32.
[12] Hartig F, Jesse U, Haußler-Combe U. Evaluation of experimental setups for determining the tensile strength of textile reinforced concrete. In: International RILEM conference on material science – MATSCI; 2010. p. 117–27.
[13] D'Ambrisi A, Focacci F, Caporale A. Strengthening of masonry-unreinforced concrete railway bridges with PBP-FRCM materials. Compos Struct 2013;107:193–204.
[14] Ombres L. Flexural analysis of reinforced concrete beams strengthened with a cement based high strength composite material. Compos Struct 2011;94(1):143–55.
[15] Capozucca R. Experimental FRP/SRP historic masonry delamination. Compos Struct 2010;92:891–903.
[16] Prochazka P, Sejnoha M. Development of debond region of lag model. Comput Struct 1995;55(2):249–60.
[17] Hartig F, Haußler-Combe U, Schicktanz K. Influence of bond properties on the tensile behaviour of textile reinforced concrete. Cement Concr Compos 2008;30(10):898–906.
[18] Carozzi G, Colombi P, Di Feo C, Montalbano A, Poggi C. The use of GFRP grids for structural rehabilitation of masonry elements. In: Proc CICE 2012, the 6th international conference on FRP composites in civil engineering, Rome, Italy, 13–15 June, 2012.
[19] Valluzzi MR et al. Round Robin Test for composite-to-brick shear bond characterization. Mater Struct 2012;45(12):1761–91. RILEM technical committee.
[20] Capozucca R. Effects of mortar layers in the delamination of GFRP bonded to historic masonry. Compos B Eng 2013;44(1):639–49.
[21] Milani G, Lourenço PB. 3D non-linear behavior of masonry arch bridges. Comput Struct 2012;110–111:133–50.
[22] Milani G, Tralli A. A simple meso-macro model based on SQP for the non-linear analysis of masonry double curvature structures. Int J Solids Struct 2012;49(5):808–34.
[23] EN ISO 10618/2005. Carbon fibre – determination of tensile properties of resin-impregnated yarn; 2005.
[24] EN 1015-11. Methods of test for mortar for masonry – determination of flexural and compressive strength of hardened mortar; 1999.
[25] Grierson DE, Franchi A, De Donato O, Corradi L. Mathematical programming and nonlinear finite element analysis. Comput Methods Appl Mech Eng 1979;17–18(PART 2):497–518.
[26] Capurso M, Maier G. Incremental elastoplastic analysis and quadratic optimization. Meccanica 1966;5(2):107–16.
[27] Kawai T. New discrete models and their application to seismic response analysis of structures. Nucl Eng Des 1978;48:207–29.